Water-wave scattering and energy dissipation by a floating porous elastic plate in three dimensions

Michael H. Meylan[a], Luke G. Bennetts[b], Malte A. Peter[c,d]

[a]*School of Mathematical and Physical Sciences, University of Newcastle, Callaghan 2308, Australia*
[b]*School of Mathematical Sciences, University of Adelaide, Adelaide 5005, Australia*
[c]*Institute of Mathematics, University of Augsburg, 86135 Augsburg, Germany*
[d]*Augsburg Centre for Innovative Technologies, University of Augsburg, 86135 Augsburg, Germany*

Abstract

An eigenfunction-matching method is developed for the problem of linear water-wave scattering by a circular floating porous elastic plate, and a coupled boundary-element and finite-element method is developed for the problem in which the plate is of arbitrary shape. The methods are shown to produce the same solutions for a circular plate, and their convergence properties are established. The impact of porosity on the far field (the wave field away from the plate) is investigated using integral representations for the Bessel and Hankel functions. It is shown that wave energy dissipation due to porosity initially increases as the plate becomes more porous, but reaches a maximum and then slowly decreases as the porosity increases further.

Keywords: Wave-Structure Interaction; Porous Elastic Plate; Eigenfunction Matching; Boundary Element Method; Finite Element Method.

1. Introduction

Porous structures are often used to dissipate water-wave energy, e.g. in breakwaters or at the end of wave flumes. Typically, single or multiple porous plates — horizontal, vertical or inclined — or rubble-mount structures are used. A major advantage of horizontal plates is that they have little effect on horizontal currents (Wang and Shen, 1999).

Water-wave interactions with fixed horizontal porous plates has been considered by many authors. Chwang and Wu (1994) solved the problem of wave reflection by a thin submerged porous circular disc. The related problem involving a porous plate of finite thickness was later solved by Neves et al. (2000). Both of these works employ eigenfunction-matching as the method of solution (using radial and axial eigenfunctions, respectively). Evans and Peter (2011) considered a thin porous plate of semi-infinite or finite length in a two-dimensional setting. They solved the semi-infinite problem analytically by the Wiener–Hopf and residue

*Corresponding author: M. H. Meylan (mike.meylan@newcastle.edu.au)

calculus techniques, using the Cauchy integral method to avoid requiring knowledge of eigenfunctions in the plate region, and the finite-length problem using a quickly convergent numerical method. Liu and Li (2011) and Liu et al. (2012) solved the two-dimensional problem using an eigenfunction-matching method, but with non-standard eigenfunctions in the plate region, thereby avoiding complicated dispersion relations at the cost of increasing the number of unknowns in the numerical solution process considerably. Cho and Kim (2013) and Cho et al. (2013) reported on comparisons with experiments conducted in a wave flume with one and two submerged porous plates, respectively.

The references above assume linear boundary conditions to be satisfied at the plate, which, in the thin plate case, enforce normal velocities of the fluid above and below the plate to be continuous and proportional to the jump in pressure across the plate based on the formulation of Chwang and Wu (1994), which, in turn, is based on the work of Taylor (1956) and Tuck (1975). An and Faltinsen (2012) considered the problem of wave interactions with a submerged porous plate with a higher-order nonlinear boundary condition for the porous plate; they also solved the associated radiation problem. It is also worth pointing out that more complex wave dissipation devices, in which a porous plate plays an integral role, have been suggested and analysed, e.g. by Wu et al. (1998), Yip and Chwang (2000), Liu et al. (2007) and Liu et al. (2008). Reviews are given by Chwang and Chan (1998), Yu (2002) and Molin (2011), discussing vertical or inclined porous structures, in addition to horizontal ones.

Similarly, the problem of water-wave diffraction by floating elastic plates has received a great deal of research attention, mainly due to its application in ocean-wave interactions with sea ice or with very large floating structures. Squire (2008) reviews literature for both communities, pointing out their connections. The solution in two dimensions was first found for a semi-infinite plate by Fox and Squire (1994) using an eigenfunction-matching method, and for a finite plate by Meylan and Squire (1994) and Newman (1994) using integral-equation formulations. The three-dimensional problem has been the subject of significantly less research. Peter et al. (2004) solved the circular-plate problem using an eigenfunction-matching method, and Bennetts et al. (2009) used a variation principle and Rayleigh–Ritz method to solve the problem when the plate is partially submerged and its thickness varies axisymmetrically. Meylan (2002) used a coupled boundary-element and finite-element method to solve the problem for an arbitrary-shape plate. Bennetts and Williams (2010) solved the arbitrary-shape plate problem by converting the governing partial differential equations to a one-dimensional system of integro-differential equations, with the restriction that the shape of the plate is smooth.

If the porous plate is thin with respect to its size but not small with respect to the wavelength it will respond elastically to the waves (also cf. Cho and Kim, 2008, for a discussion of the associated disadvantages in using vertical porous plates). Therefore, it is an obvious question how to compute the wave response of a porous elastic plate. Some literature involving porous elastic plates is available. Wang and Ren (1993) and Yip et al. (2002) considered theoretically reflection and transmission by a thin vertical porous plate. Similar problems were considered recently by Koley et al. (2015) and Kaligatla et al. (2015), and by Mandal et al. (2015) for multiple structures. Related problem involving vertical porous elas-

tic membranes instead of plates were considerd by Kumar and Sahoo (2006) and Williams and Wang (2007). Finally, Behera and Sahoo (2015) solved the problem of a submerged elastic porous plate. However, all of these works are in the two-dimensional setting, i.e. one horizontal and one vertical dimension. Particularly for applications involving ocean waves, a three-dimensional consideration is required.

It turns out that the wave response of a porous thin elastic plate in three dimensions can be computed by the extension of powerful methods available for elastic plates. Two methods are showcased for the case of a floating porous elastic plate. The first method considered is an eigenfunction-matching method, in the case that the plate is circular. The second method is a coupled boundary-element and finite-element method, which accommodates plates of arbitrary shape. It should be noted that the results presented here could be extended to multiple porous thin elastic plates using the method outlined by Peter and Meylan (2004) for thin elastic plates.

The general problem and the solution methods are outlined in §§ 2–4. Convergence rates of the methods with respect to truncations employed in them are investigated, and examples of the plate displacements are shown, indicating the damping caused by porosity. The displacements produced by the eigenfunction-matching method and the coupled boundary-element and finite-element method for circular plates are shown to agree, providing validation of the methods. In § 5, the far-field amplitude of the wave field is derived, and used to determine the wave energy dissipated due to porosity. It is shown that energy dissipation initially increases with increasing porosity, but then slowly decreases.

2. Equations of motion

Consider a three-dimensional water domain, extending to infinity in all horizontal directions and with finite depth. Locations in the water are defined by the Cartesian coordinate system (x, y, z), where $\mathbf{x} \equiv (x, y)$ is the horizontal coordinate and z is an upward-pointing vertical coordinate. The water is bounded below by a flat impermeable bed at $z = -H$, and above by a free surface $z = \eta(x, y, t)$. The origin of the vertical coordinate is set to coincide with the equilibrium location of the free surface, i.e. $\eta = 0$ when the system is at rest.

The water is assumed to be homogeneous, inviscid and incompressible, and its motion irrotational and time-harmonic with a prescribed real angular frequency ω. Therefore, the water velocity field is defined as $\mathrm{Re}\{(g/\mathrm{i}\omega)\phi(x, y, z)\mathrm{e}^{-\mathrm{i}\omega t}\}$, where Re denotes the real part of the included quantity, t is time, $g \approx 9.81\,\mathrm{m\,s^{-2}}$ is the constant of gravitational acceleration, and the scalar function ϕ is a complex-valued velocity potential.

A thin, flexible, porous plate of uniform thickness h floats on the water surface, and is set in motion by a plane incident wave. Kirchoff–Love thin-plate theory, modified to include porosity, is used to model the plate motions. Therefore, the flexural motions of the plate are defined in terms of the vertical displacements of its lower surface, denoted $z = \mathrm{Re}\{w(x, y)\mathrm{e}^{-\mathrm{i}\omega t}\}$ for $(x, y) \in \Omega \subset \mathbb{R}^2$, where Ω is the orthogonal projection of the plate onto the horizontal plane.

Linear theory is employed, on the basis of the wave elevation and plate displacements being small perturbations from the equilibrium, with respect to the horizontal lengths (small

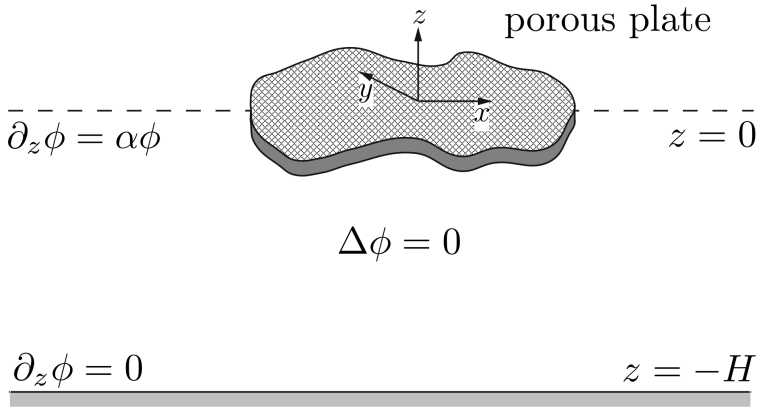

Figure 1: Schmatic of the geometry.

wave steepness) and vertical lengths (small wave amplitudes relative to the water depth). It follows that the velocity potential satisfies Laplace's equation in the linearised water domain

$$\Delta\phi = 0 \quad \text{for} \quad \mathbf{x} \in \mathbb{R}^2 \quad \text{and} \quad -H < z < 0, \tag{1a}$$

where $\Delta \equiv \partial_x^2 + \partial_y^2 + \partial_z^2$ is the Laplacian operator, and the impermeable-bed condition

$$\partial_z\phi = 0 \quad \text{for} \quad \mathbf{x} \in \mathbb{R}^2 \quad \text{and} \quad z = -H. \tag{1b}$$

On the linearised free surface away from the plate, the velocity potential and surface elevation, η, are related through dynamic and kinematic conditions. These are combined to eliminate η, leaving the free-surface condition

$$\partial_z\phi = \alpha\phi \quad \text{for} \quad \mathbf{x} \notin \Omega \quad \text{and} \quad z = 0, \tag{1c}$$

where $\alpha = \omega^2/g$ is a frequency parameter.

Assuming all points on the lower surface of the plate remain in contact with the water during its motion, the velocity potential, ϕ, is coupled to the plate displacement function, w, via kinematic and dynamic conditions, respectively

$$\partial_z\phi = \alpha w + \mathrm{i}P\phi \qquad \text{and} \qquad \phi = w + \beta\Delta_{\mathbf{x}}^2 w - \alpha\gamma w \tag{2a}$$

for $\mathbf{x} \in \Omega$ and $z = 0$. Here, $\Delta_{\mathbf{x}} \equiv \partial_x^2 + \partial_y^2$ is the Laplacian operator in the horizontal plane, γ is the mass per unit area of the plate scaled with respect to the water density, and β is the flexural rigidity of the plate scaled with respect to the water density. Porosity is included in the model through the second term on the right-hand side of the first component of Eqn. (2a), derived from Darcy's law and assuming constant atmospheric pressure normalised to zero. The porosity parameter $P = \omega K\rho/(\mu h)$, where ρ and μ are the density and dynamic viscosity of water, respectively, and K is the permeability of the plate, will act as the independent variable for this study. The edge of the plate is unrestrained — the bending moment and shearing stress vanish there — providing the conditions

$$\Delta_{\mathbf{x}} w - (1-\nu)\{\partial_s^2 w + \Theta'\partial_n w\} = 0 \quad \text{and} \quad \partial_n\Delta_{\mathbf{x}} w + (1-\nu)\partial_s\partial_n\partial_s w = 0 \tag{2b}$$

for $\mathbf{x} \in \partial\Omega$, the boundary of Ω. Here ν is Poison's ratio and ∂_n is the differential operator corresponding to the normal vector $\mathbf{n} = (\cos\Theta, \sin\Theta)$, where Θ is a function of the parameter s defining locations on the boundary (cf. Bennetts et al., 2007).

Eqns. (1) and (2) constitute a boundary-value problem for the velocity potential, ϕ, and displacement function, w. The problem may be recast so that the velocity potential is the only independent variable, by combining the two components of Eqn. (2a) into

$$\phi = \left\{1 - \alpha\gamma + \beta\Delta_{\mathbf{x}}^2\right\}(\partial_z\phi - \mathrm{i}P\phi) \quad \text{for} \quad \mathbf{x} \in \Omega \quad \text{and} \quad z = 0, \tag{3}$$

and expressing the free-edge conditions (2b) in a similar manner.

In the far-field, $r \gg 1$, where $r \equiv |\mathbf{x}|$ is the radial coordinate, the solution is subject to the Sommerfeld radiation condition

$$r^{1/2}\left\{\partial_r\phi^{\mathrm{sc}} - \mathrm{i}k_0\phi^{\mathrm{sc}}\right\} \to 0 \quad \text{as} \quad r \to \infty, \tag{4}$$

uniformly in the azimuthal coordinate $\theta \equiv \arctan(y/x)$. Here $\phi^{\mathrm{sc}} = \phi - \phi^{\mathrm{in}}$ is the scattered wave potential, where

$$\phi^{\mathrm{in}} = A\mathrm{e}^{\mathrm{i}k_0(x\cos\psi + y\sin\psi)}\xi_0(z) \qquad \text{with} \qquad \xi_0(z) = \frac{\cosh k_0(z+H)}{\cosh k_0 H}, \tag{5}$$

is the velocity potential of a plane incident wave with amplitude A and travelling at the angle ψ with respect to the positive x-axis. The wave number k_0 is calculated from α using the dispersion equation which is given in the following section.

3. Eigenfunction-matching method for a circular plate

Consider a circular plate of radius a, i.e. $\Omega = \{\mathbf{x} : |\mathbf{x}| < a\}$. In this case, the geometry is separable with respect to the cylindrical polar coordinate system (r, θ, z), resulting in the eigenfunction expansions

$$\phi = \phi^{\mathrm{in}} + \sum_{n=0}^{\infty}\sum_{m=-\infty}^{\infty} a_{n,m}\mathrm{H}_m(k_n r)\mathrm{e}^{\mathrm{i}m\theta}\xi_n(z) \quad \text{for} \quad \mathbf{x} \notin \Omega \quad \text{and} \quad -H < z < 0, \tag{6a}$$

$$\text{and} \quad \phi = \sum_{n=-2}^{\infty}\sum_{m=-\infty}^{\infty} b_{n,m}\mathrm{J}_m(k_n r)\mathrm{e}^{\mathrm{i}m\theta}\zeta_n(z) \quad \text{for} \quad \mathbf{x} \in \Omega \quad \text{and} \quad -H < z < 0, \tag{6b}$$

where J_m and H_m are order-m Bessel and Hankel functions of the first kind, respectively,

$$\xi_n(z) = \frac{\cosh k_n(z+H)}{\cosh k_n H} \qquad \text{and} \qquad \zeta_n(z) = \frac{\cosh \kappa_n(z+H)}{\cosh \kappa_n H}. \tag{7}$$

The open-water wave numbers k_n for $n = 0, 1, \ldots$ are the roots k of the dispersion relation

$$k\tanh(kH) = \alpha, \tag{8}$$

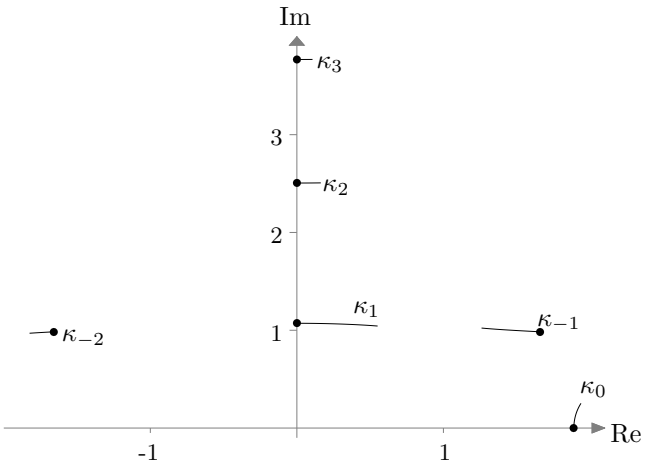

Figure 2: Loci of the plate-covered wave numbers κ_n for $n = -2, \ldots, 3$ in the complex plane, for $PH \in [0, 1]$, with $\alpha H = 2$ and $\beta/H^4 = \gamma H = 0.01$. Bullets indicate locations for $PH = 0$.

where $k_0 \in \mathbb{R}^+$ supports propagating waves, and $k_n \in \mathrm{i}\mathbb{R}^+$ for $n = 1, 2, \ldots$ support evanescent waves. The plate-covered wave numbers κ_n for $n = -2, -1, \ldots$ are the roots κ of the dispersion relation

$$(\beta\kappa^4 + 1 - \alpha\gamma)(\kappa \tanh(\kappa H) + \mathrm{i}P) = \alpha. \tag{9}$$

For $P = 0$, similarly to the open-water case, $\kappa_0 \in \mathbb{R}^+$ supports propagating waves, and $\kappa_n \in \mathrm{i}\mathbb{R}^+$ for $n = 1, 2, \ldots$ support evanescent waves. As these wave numbers lie on the real or imaginary axes of the complex plane, they may be calculated, for example, using a bisection method. The two additional roots are, in general, such that $\kappa_{-1} \in \mathbb{R}^+ + \mathrm{i}\mathbb{R}^+$ and $\kappa_{-2} = -\overline{\kappa_{-1}}$, i.e. they are symmetric in the complex plane with respect to the imaginary axis, supporting damped propagating waves. These wave numbers may be calculated, for example, using Newton's method.

For $P \neq 0$, the structure of the wave numbers is perturbed, with κ_0 obtaining a positive imaginary component, damping the propagating wave and resulting in energy loss. The purely imaginary wave numbers, κ_n for $n = 1, \ldots,$ obtain real components, and κ_{-1} and κ_{-2} lose their symmetry. The roots in this case are calculated using a homotopy method, starting with the corresponding roots for the zero-porosity case and incrementing the porosity parameter to the specified value. Fig 2 shows an example of the loci of κ_n for $n = -2, \ldots, 3$ in the complex plane with $P \in [0, 1]$. The parameter values used for this example (non-dimensionalised with respect to the water depth, H) are $\alpha H = 2$ and $\beta/H^4 = \gamma H = 0.01$. These values are maintained for the remainder of the study.

The amplitudes of the scattered waves, $b_{n,m}$, and the waves in the plate-covered region, $a_{n,m}$, are calculated using an eigenfunction-matching method. Expressions (6) for the velocity potential are equated at the interface between the open-water and plate-covered regions, $\mathbf{x} \in \partial\Omega$ and $-H < z < 0$, providing continuity of pressure, and their radial derivatives are equated, providing continuity of radial velocity. These continuity conditions are

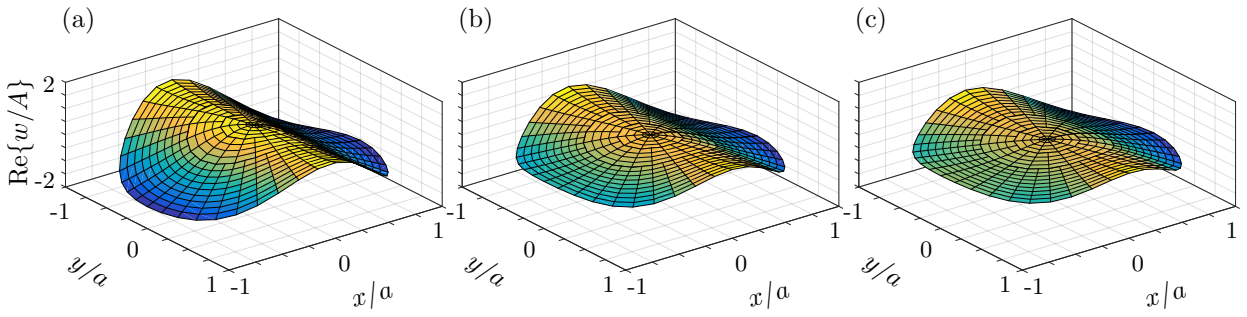

Figure 3: Example displacements of circular plate at $t = 0$ calculated using the eigenfunction-matching method, for non-dimensional radius $a/H = 2$, incident-wave direction $\psi = 0$ and porosity parameter (a) $PH = 0$, (b) $PH = 0.5$, and (c) $PH = 1$.

mapped to a linear system of equations by taking inner-products with respect to the vertical eigenfunctions ξ_n for $n = 0, \ldots$. For numerical calculation, all infinite series of vertical eigenfunctions are truncated at N and azimuthal eigenfunctions at $\pm M$, where N and M are chosen sufficiently large to provide a desired level of accuracy. The free-edge conditions (2b) are appended to the system to close it, using the eigenfunction expansion (6b). Noting that the incident wave can be expressed

$$\phi^{\text{in}} = \sum_{m=-\infty}^{\infty} \mathrm{e}^{\mathrm{i}m(\pi/2-\psi)} \mathrm{J}_m(k_0 r) \mathrm{e}^{\mathrm{i}m\theta} \xi_0(z), \tag{10}$$

and, for the circular geometry, that the free-edge conditions reduce to

$$\left\{ \Delta_{r,\theta} - \frac{1-\nu}{r} \left(\partial_r + \frac{1}{r} \partial_\theta^2 \right) \right\} w = 0 \quad \text{and} \quad \left\{ \partial_r \Delta_{r,\theta} - \frac{1-\nu}{r^2} \left(\partial_r + \frac{1}{r} \right) \partial_\theta^2 \right\} w = 0 \tag{11}$$

for $r = a$, where $\Delta_{r,\theta} \equiv \partial_r^2 + r^{-1}\partial_r + r^{-2}\partial_\theta^2$, the azimuthal modes decouple, i.e. the system for each azimuthal mode $m \in \{-M, \ldots, M\}$ is solved separately.

Fig. 3 shows three examples of plate displacements at $t = 0$, $\mathrm{Re}\{w\}$, produced by incident waves travelling in the direction of the positive x-axis, $\psi = 0$. One example is for zero porosity and the other two are for non-zero porosity. The non-dimensional radius of the plate is $a/H = 2$, with this value maintained for the remainder of the study. Truncations $M = N = 10$ are used to calculate the displacements. The shape of the displacements are dominated by the plane incident wave. Porosity damps the displacements, particularly at the centre of the plate.

Fig. 4 shows the convergences of the eigenfunction-matching method with respect to the truncations of the vertical and azimuthal eigenfunctions. Convergences are quantified by L_2-norms of the differences between successive approximations of the displacement function, respectively,

$$\delta w_N^{\text{vt}} = \left(\iint_\Omega \left| \frac{w^{(N,M)} - w^{(N-1,M)}}{A} \right|^2 \mathrm{d}\mathbf{x} \right)^{\frac{1}{2}} \tag{12a}$$

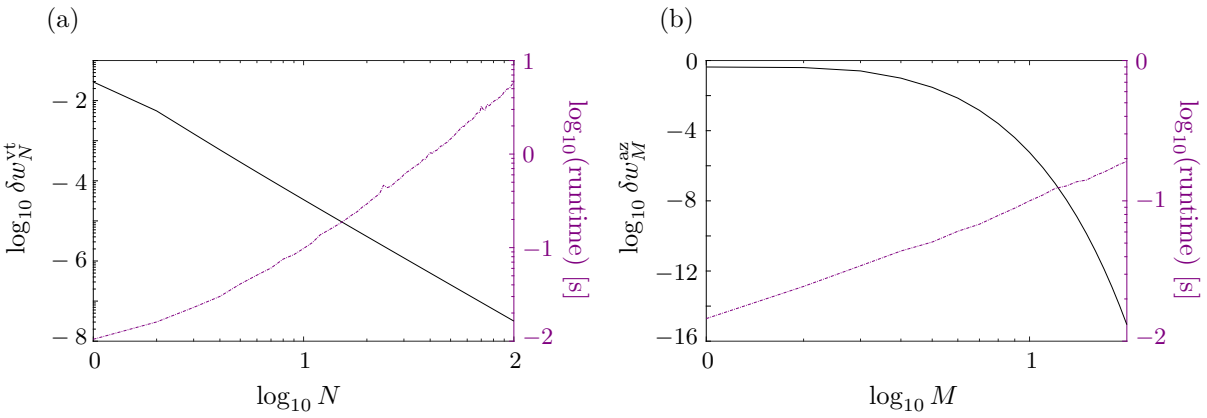

Figure 4: Convergences of the eigenfunction-matching method (−) and computational runtimes (---), with respect to truncations of (a) vertical eigenfunctions, N, with $M = 10$, and (b) azimuthal eigenfunctions, M, with $N = 10$.

$$\text{and} \quad \delta w_M^{\mathrm{az}} = \left(\iint_\Omega \left| \frac{w^{(N,M)} - w^{(N,M-1)}}{A} \right|^2 \mathrm{d}\mathbf{x} \right)^{\frac{1}{2}}, \tag{12b}$$

where $w^{(N,M)}$ denotes the displacement function for vertical truncation N and azimuthal truncation M. The corresponding computational runtimes are superimposed on the plots.

Results are shown for the zero-porosity case of Fig. 3. The convergence rate with respect to the vertical eigenfunctions is M^{-3}. The convergence rate with respect to the azimuthal eigenfunctions is exponential, presumably because the incident forcing (10) drops off exponentially with respect to azimuthal order at $r = a$. Convergence rates are identical for non-zero porosity cases tested, although the difference between successive approximations are smaller due to the smaller displacements. The runtimes increase at a rate of approximately $N^{1.8}$ with respect to the vertical eigenfunctions, as the azimuthal modes are decoupled. The runtimes for non-zero porosities are slightly longer due to the homotopy method used to calculate the perturbed wave numbers.

4. Coupled boundary-element and finite-element method for an arbitrary-shape plate

The solution for a non-circular plate is found using a very different method based on a coupled boundary-element and finite-element method. In this method, the plate motion is expanded in modes of free vibration — the standard method for solving complex hydroelastic problems. The expansion is

$$w = \sum_{j=1}^{\infty} u_j w_j \tag{13}$$

with coefficients u_j, where the modes $w_j(\mathbf{x})$, $j = 1, 2, \ldots$, satisfy the eigenvalue problem for the biharmonic operator,

$$\Delta_{\mathbf{x}}^2 w_j = \mu_j^4 w_j \qquad \text{for} \qquad \mathbf{x} \in \Omega, \tag{14}$$

together with the free-edge conditions (2b), where μ_j^4 are the eigenvalues numbered in ascending order of their magnitude. The modes represent the free vibrational modes of the plate in vacuo and they depend on the shape of the plate only. Since the operator $\Delta_{\mathbf{x}}^2$ subject to the free-edge boundary conditions is self-adjoint the eigenspaces are orthogonal for different eigenvalues. We form an othornormal basis for these eigenspaces numbered with increasing eigenvalue in the normal way, i.e.

$$\iint_\Omega w_i(\mathbf{x}) w_j(\mathbf{x}) \, \mathrm{d}\mathbf{x} = \delta_{ij}, \tag{15}$$

where δ_{ij} is the Kronecker delta. The eigenfunctions are calculated using the finite element method as outlined by Meylan (2002). Inserting expansion (13) into Eqns. (2) gives

$$\partial_z \phi = \sum_{j=1}^{\infty} u_j w_j + \mathrm{i} P \phi, \qquad \text{for} \quad \mathbf{x} \in \Omega \quad \text{and} \quad z = 0, \tag{16a}$$

$$\phi = \sum_{j=1}^{\infty} \left(1 + \beta \mu_j^4\right) u_j w_j - \alpha\gamma \sum_{j=1}^{\infty} u_j w_j, \qquad \text{for} \quad \mathbf{x} \in \Omega \quad \text{and} \quad z = 0. \tag{16b}$$

By linearity, the velocity potential is expanded as

$$\phi = \phi^{\mathrm{in}} + \phi^{\mathrm{di}} - \sum_{j=1}^{\infty} u_j \phi_j^{\mathrm{ra}}, \tag{17}$$

where ϕ^{in} is the incident wave potential, cf. Eqn. (5). The sum of the incident wave and diffraction potentials, $\phi^{\mathrm{in}} + \phi^{\mathrm{di}}$, is the solution of the problem in which the plate is held in place. The radiation potentials, ϕ_j^{ra}, $j = 1, 2, \ldots$, are solutions of the problems in which the plate oscillates in one of its free modes with unit amplitude.

On the linearised water surface, $z = 0$, the diffraction and radiation potentials can be expressed as

$$\phi^{\mathrm{di}}(\mathbf{x}, 0) = \iint_\Omega G(\mathbf{x}, 0; \mathbf{x}') \left(\alpha \left(\phi^{\mathrm{in}}(\mathbf{x}', 0) + \phi^{\mathrm{di}}(\mathbf{x}', 0)\right) - \mathrm{i} P \left(\phi^{\mathrm{in}}(\mathbf{x}', 0) + \phi^{\mathrm{di}}(\mathbf{x}', 0)\right)\right) \, \mathrm{d}\mathbf{x}', \tag{18a}$$

$$\phi_j^{\mathrm{ra}}(\mathbf{x}, 0) = \iint_\Omega G(\mathbf{x}, 0; \mathbf{x}') \left(\alpha \phi_j^{\mathrm{ra}}(\mathbf{x}', 0) - \mathrm{i} P \phi_j^{\mathrm{ra}}(\mathbf{x}', 0) - w_j(\mathbf{x}')\right) \, \mathrm{d}\mathbf{x}', \quad j = 1, 2, \ldots \tag{18b}$$

Here, $G(\mathbf{x}, z; \mathbf{x}')$ is the free surface Green's function for a point source located at the water surface, which can be expressed as

$$G = \sum_{n=0}^{\infty} \frac{\mathrm{i} \cosh k_n H}{4 H N_n^2} \cosh k_n (z + H) \mathrm{H}_0(k_n R), \quad \text{where} \quad N_n^2 = \frac{1}{2} \left(1 + \frac{\sinh 2k_n H}{2k_n H}\right), \tag{19}$$

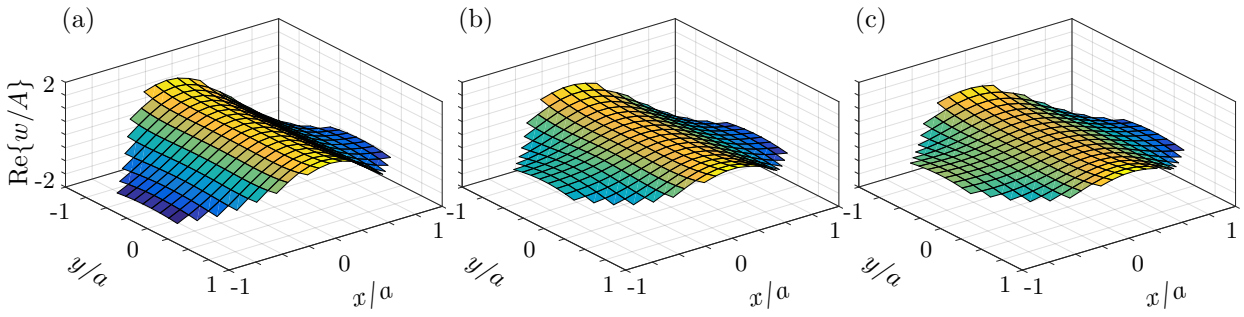

Figure 5: Displacements of circular plates calculated, as in Fig. 3, but computed with the coupled boundary-element and finite-element method, which approximates the circular shape with square panels.

R is the distance of the field point from the source point and k_m are the roots of the dispersion relation (8) (cf., e.g., Linton and McIver, 2001, Eqn. B.91). Expressions (18) are solved for $\mathbf{x} \in \Omega$ using a constant panel method (see Meylan, 2002).

A linear system for the modal weights $\boldsymbol{u} = [u_i]_i$ is obtained by applying the dynamic coupling condition (16b) to the expanded velocity potential (17) and taking inner products with respect to the free vibrational modes of the plate. After truncation of the number of modes, the system is expressed in matrix form as

$$\big(\mathbf{K} + \mathbf{C} - \alpha\mathbf{M} - \omega^2\mathbf{A}(\omega) - \mathrm{i}\omega\mathbf{B}(\omega)\big)\,\boldsymbol{u} = \mathbf{f}(\omega). \tag{20}$$

Here $\mathbf{K}$, $\mathbf{M}$ and $\mathbf{C}$ are stiffness, mass and hydrostatic-restoring matrices, respectively. They are given by

$$\mathbf{K} = \lceil \beta\mu_j^4 \rfloor_j, \qquad \mathbf{M} = \gamma\mathbf{I} \qquad \text{and} \qquad \mathbf{C} = \mathbf{I}, \tag{21}$$

where $\lceil c_i \rfloor_i$ denotes a diagonal matrix with diagonal entries c_i, and $\mathbf{I}$ is the identity matrix. Moreover, the elements of the real added mass matrix $\mathbf{A} = [A_{ij}]_{ij}$ and real damping matrix $\mathbf{B} = [B_{ij}]_{ij}$ are defined as

$$\omega^2 A_{ij} + \mathrm{i}\omega B_{ij} = -\iint_\Omega \phi_j^{\mathrm{ra}} w_i \,\mathrm{d}S, \tag{22}$$

and the elements of the forcing vector $\mathbf{f} = [f_i]_i$ are given by

$$f_i = \iint_\Omega \left(\phi^{\mathrm{in}} + \phi^{\mathrm{di}}\right) w_i \,\mathrm{d}S. \tag{23}$$

Fig. 5 shows three examples of the displacement of a circular plate, calculated using the coupled boundary-element and finite-element method, in direct analogy to Fig. 3 for validation. Even though the circular shape is approximated by square panels, the displacements compare very well.

Fig. 6 shows example displacements of porous plates at $t = 0$, for three different plate shapes: a square, a right-angled triangle and a rhombus. The shapes are the maximum

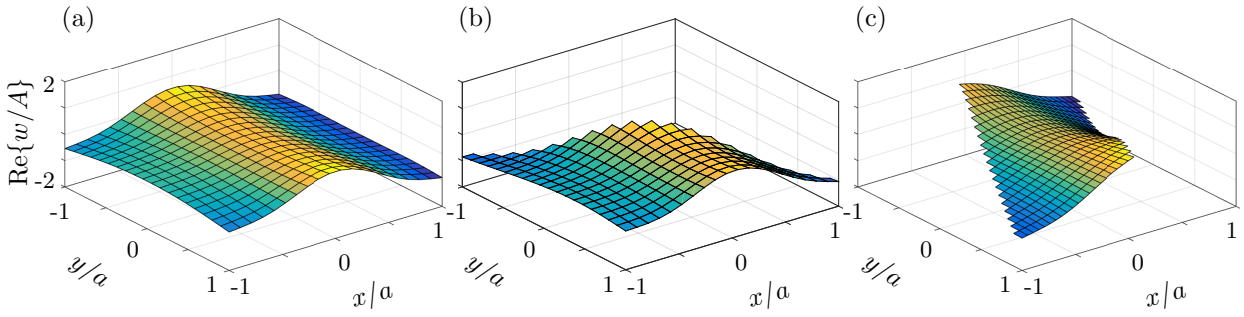

Figure 6: Example displacements of (a) square, (b) triangular and (c) rhombic plates, for porosity parameter $PH = 0.5$ and incident angle $\psi = 0$.

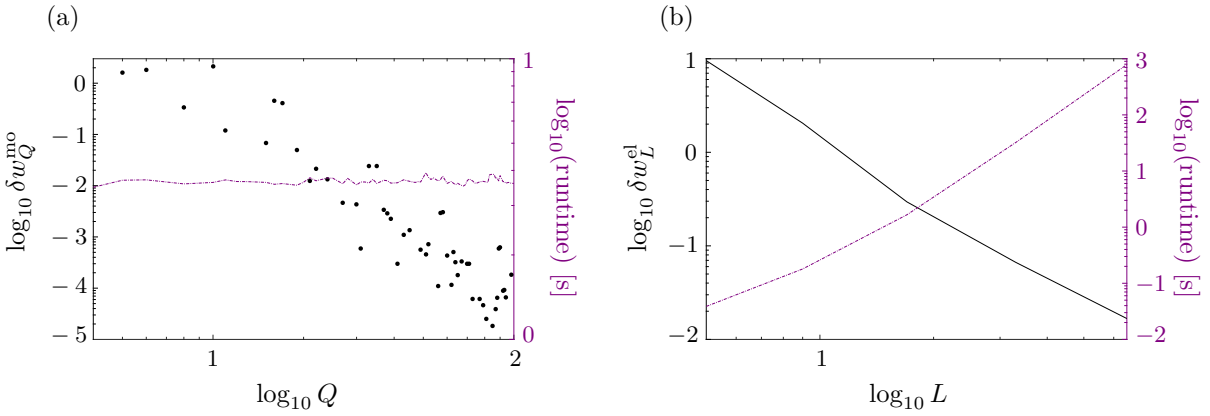

Figure 7: Convergences of the coupled boundary-element and finite-element method (•, −) and computational runtimes (---), with respect to truncations of (a) number of radiation potentials (i.e. number of free vibrational modes), Q, with $L = 20$, and (b) number of points in the discretisation of each side of the plate, L, with $Q = 25$.

sizes of their type fitting into the bounding box for the circular plate, i.e. a square with side lengths of $2a$. It can be seen that their responses to the incident wave are all quite similar for the parameter values chosen.

Fig. 7 shows the convergence behaviour of the coupled boundary-element and finite-element method for the square plate with zero porosity. Denoting by Q the truncation value for the number of radiation potentials (i.e. the number of free vibrational modes) used in the computation and by L the number of points in the discretisation of each side of the plate, convergence is quantified by L_2-norms of the differences between successive approximations of the displacement function, respectively,

$$\delta w_Q^{\mathrm{mo}} = \left(\iint_\Omega \left| \frac{w^{(Q,L)} - w^{(Q-1,L)}}{A} \right|^2 \, \mathrm{d}\mathbf{x} \right)^{\frac{1}{2}} \tag{24a}$$

$$\text{and} \quad \delta w_L^{\mathrm{el}} = \left(\iint_\Omega \left| \frac{w^{(Q,L)} - w^{(Q,(L+1)/2)}}{A} \right|^2 \, \mathrm{d}\mathbf{x} \right)^{\frac{1}{2}}, \tag{24b}$$

where $w^{(Q,L)}$ denotes the displacement function for modal truncation Q and spatial discretisation L. Note that only $Q \geq 4$ is considered in order to include at least the rigid-body heave, pitch and roll modes and that the number of panels is given by L^2 for the square plate. The corresponding computational runtimes are superimposed on the plots.

The convergence rate with respect to the free vibrational modes is very rapid beyond $Q \sim 10$, suggesting that high frequency vibrational modes are hardly excited by the (low-frequency) incident wave. It is interesting to note that the quantity $w^{(Q,L)}$ drops very close to zero occasionally and this can be attributed to: (i) symmetry of the square plate causing some modes appear in pairs that have to be added to the computation simultaneously in order to increase accuracy; and (ii) modes not being excited in the square plate by the normally incident wave. The runtime is hardly affected by the number of modes as the main part of the computational time is in the boundary-element part. The convergence with respect to number of points in the discretisation of each side of the plate is roughly L^{-3}. Note that the increase in runtime is considerable. Again, the results for non-zero porosities are very similar. Wang and Meylan (2004) provide a more comprehensive convergence study of the coupled boundary-element and finite-element method for the non-porous elastic plate.

5. Far-field amplitude and energy dissipation

The evanescent wave components of the scattered wave field decay exponentially away from the plate, leaving only the propagating wave component. For the circular plate, the scattered wave potential, ϕ^{sc}, reduces to

$$\phi^{\mathrm{sc}} \sim \sum_{m=-\infty}^{\infty} a_{0,m} \mathrm{H}_m(k_0 r) \mathrm{e}^{\mathrm{i}m\theta} \xi_0(z) \quad \text{in the far field} \quad r \gg 1. \tag{25}$$

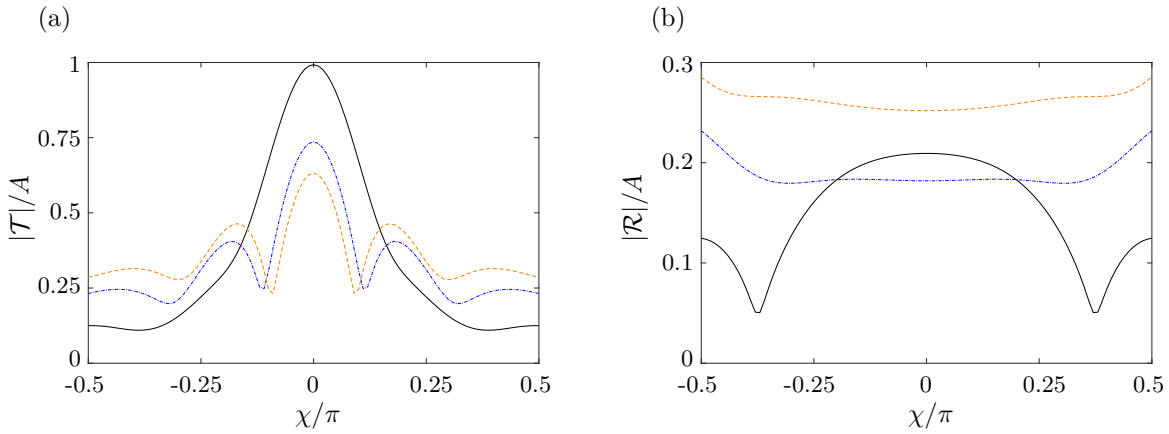

Figure 8: Moduli of (a) transmitted and (b) reflected amplitude functions for the circular plate, produced by the continuous incident amplitude $\mathcal{A} = A\cos^{16}\chi$, for $PH = 0$ (−), $PH = 0.5$ (---) and $PH = 1$ (--).

Following Montiel et al. (2015a,b), this potential can be expressed as an integral of plane waves,

$$\phi^{\mathrm{sc}} \sim \int_{\mathcal{C}} \mathcal{D}(\chi)\mathrm{e}^{\mathrm{i}k_0 r\cos(\theta-\chi)}\,\mathrm{d}\chi\;\xi_0(z) \quad \text{for} \quad r \gg 1, \tag{26}$$

where the integral contour $\mathcal{C}(\theta) = (-\pi/2, \pi/2) + \theta$, and $\mathcal{D}$ is the amplitude function of the scattered wave field with respect to the directional spectrum. The amplitude function is related to the standard far-field amplitude D, defined by

$$\phi^{\mathrm{sc}} \sim \sqrt{\frac{2}{\mathrm{i}\pi kr}}D(\theta)\mathrm{e}^{\mathrm{i}k_0 r}\xi_0(z) \quad \text{for} \quad r \gg 1, \quad \text{and} \quad D(\theta) = \sum_{m=-\infty}^{\infty} a_{0,m}\mathrm{e}^{\mathrm{i}m(\theta-\pi/2)}, \tag{27}$$

simply by $\mathcal{D} = D/\pi$.

The incident wave potential is written as the integral of plane waves

$$\phi^{\mathrm{in}} = \int_{-\pi/2}^{3\pi/2} \mathcal{A}(\chi)\mathrm{e}^{\mathrm{i}k_0 r\cos(\theta-\chi)}\,\mathrm{d}\chi\;\xi_0(z), \tag{28}$$

where, for the plane incident wave at angle ψ given in Eqn. (5), the amplitude function $\mathcal{A}(\chi) = A\delta(\chi-\psi)$, with δ the Dirac delta distribution. Reflected and transmitted amplitude functions are defined, respectively, as

$$\mathcal{R}(\chi) = \mathcal{D}(\psi+\chi+\pi) \quad \text{and} \quad \mathcal{T}(\chi) = \mathcal{A}(\psi+\chi) + \mathcal{D}(\psi+\chi) \quad \text{for} \quad \chi \in (-\pi/2, \pi/2)\,, \tag{29}$$

where arguments are understood to be modulo 2π and in the appropriate interval.

Fig. 8 shows absolute values of transmitted and reflected amplitude functions for the non-porous plate and porous plates with $P = 0.5$ and 1. For presentational purposes, the continuous function $\mathcal{A} = A\cos^{16}\chi$ is used for the incident amplitude, providing an integral of plane incident waves in a narrow band around the positive x-direction. Following

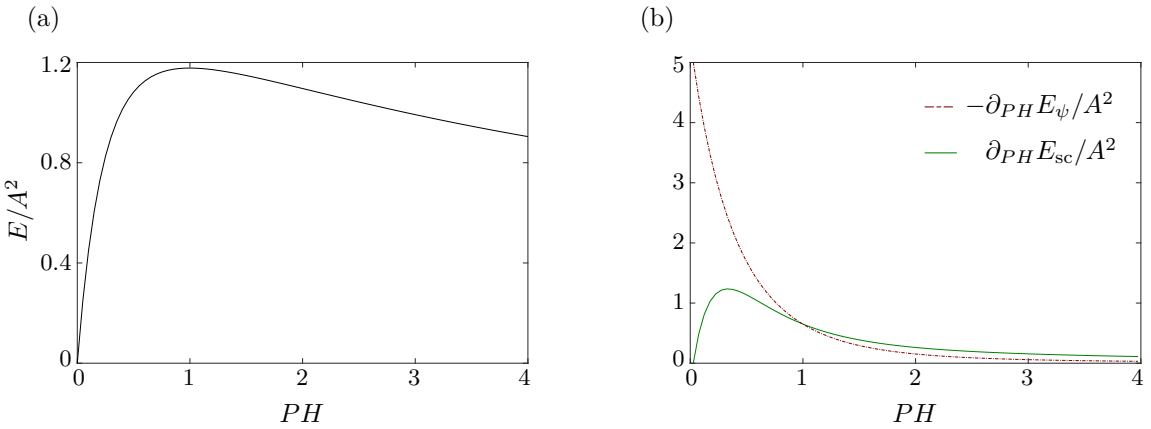

Figure 9: (a) Wave energy dissipated due to porosity, as a function of the porosity parameter, for the circular plate. (b) Derivatives, with respect to the porosity parameter, of the energy transmitted in the incident wave direction (---) and scattered in all other directions (—).

Montiel et al. (2015a), the transmitted and reflected amplitude functions for a continuous incident amplitude are calculated at sampled points in the directional spectrum using sampled reflection and transmission kernels, with 101 uniformly distributed points in the interval $(-\pi/2, \pi/2)$ used for these results.

The wave field transmitted by the non-porous plate is dominated by the incident spectrum. Porosity damps transmission in the direction of the incident field, with the damping increasing as the porosity parameter increases but the rate of increase slowing. The porosity creates side bands around the incident direction in the transmitted field, causing the amplitudes of the waves in these directions to exceed those for the non-porous plate.

The wave field reflected by the non-porous plate peaks in the direction opposite to the incident wave direction. Porosity smoothes the reflected spectrum, producing a net increase in the reflected amplitude, presumably due to a greater impedance mismatch between open water and the plate-covered water when porosity is introduced. The mean of the reflected amplitude increases as the porosity parameter becomes larger.

Fig. 9(a) shows the quantity

$$E = \int_{-\pi/2}^{3\pi/2} |\mathcal{A}(\chi)|^2 \, \mathrm{d}\chi - \int_{-\pi/2}^{3\pi/2} |\mathcal{A}(\chi) + \mathcal{D}(\chi)|^2 \, \mathrm{d}\chi, \tag{30}$$

which is proportional to the energy dissipated due to porosity, as a function of the porosity parameter. For the purpose of numerical calculations, the incident amplitude function is approximated as

$$\mathcal{A}(\chi) \approx \frac{A}{2\pi} \sum_{m=-100}^{100} \mathrm{e}^{\mathrm{i}m(\chi-\psi)}, \tag{31}$$

i.e. a truncated version of the (formal) Fourier series for the delta distribution. For non-dimensionalised porosity parameter, PH, less than approximately unity, dissipation increases with increasing porosity, as expected. As indicated in Fig. 8(a), the increase in

dissipation with respect to the porosity parameter is initially rapid, but levels off as PH approaches unity. For PH greater than unity, dissipation decreases as the porosity increases. This is not surprising, since if the porosity vanishes then the problem conserves energy and if the porosity is large then the boundary condition under the plate becomes approximately $\phi = 0$, which is also energy conserving.

Fig. 9(b) shows the corresponding derivatives of the quantities

$$E_\psi = \int_{\psi-\varepsilon/2}^{\psi+\varepsilon/2} |\mathcal{T}|^2 \quad \text{and} \quad E_{\text{sc}} = \int_{-\pi/2}^{3\pi/2} |\mathcal{R}|^2 + |\mathcal{T}|^2 \, \mathrm{d}\chi - E_\psi, \tag{32}$$

where ε is the distance between sampled points in the directional spectrum, with respect to the porosity parameter. The quantites E_ψ and E_{sc} represent the energy transmitted in the incident wave direction and scattered in all other directions, respectively. As indicated in Fig. 8, the transmitted energy in the incident wave direction decreases as the porosity increases, whereas the energy in the other directions increases as the porosity increases. For PH less than unity the decrease in transmission outweighs the increase in scattering, but for PH greater than unity the opposite is true, explaining the rollover in the energy with respect to the porosity parameter shown in Fig. 9(a).

For an arbitrary-shape plate, the far-field amplitude, D, is defined as

$$D(\theta) = \frac{\mathrm{i}(k_0^2 - \alpha^2)\cosh^2(k_0 H)}{2\{H(k_0^2 - \alpha^2) + \alpha\}} K(\theta), \tag{33}$$

where K is the Kochin function

$$K(\theta) = \iint_\Omega \Big(\alpha w - (\alpha - \mathrm{i}P)\phi\Big) \mathrm{e}^{-\mathrm{i}k_0(x' \cos\theta + y' \sin\theta)} \, \mathrm{d}\mathbf{x}', \tag{34}$$

(see Mei et al., 2005, § 8.4, for details of the non-porous, rigid case).

Fig. 10(a) shows the modulus of the scattered amplitude function, $\mathcal{D}$, for the circular plate with porosity $PH = 0.5$, in response to a plane incident wave at angle $\psi = \pi/6$, calculated using the coupled boundary-element and finite-element method, and also for the plates shown in Fig. 6. The amplitudes peak in the direction of the incident wave for all plate shapes, with the square plate attaining the maximum amplitude. The peak of the rhombic plate shows significant asymmetry, with the peaks for the other plates approximately symmetric. The amplitude functions for all shapes possess side bands around the main peak, with maxima approximately $\pm\pi$ from the incident wave direction. For the square and triangular plates, the side band above the main peak are wider than below it, and the triangular plate produces an additional peak in approximately the opposite direction to the incident wave.

Fig. 10(b) shows the energy dissipated by the different shaped plates, as functions of the porosity parameter. For the circular plate, results calculated by the eigenfunction-matching and the coupled boundary-element and finite-element methods are provided, validating the two approaches. The dissipation behaviours are consistent for the different plate shapes — as shown in Fig. 9(a) for the circular plate, dissipation initially increases rapidly with increasing porosity, reaching a maximum and then slowly decreasing as porosity further

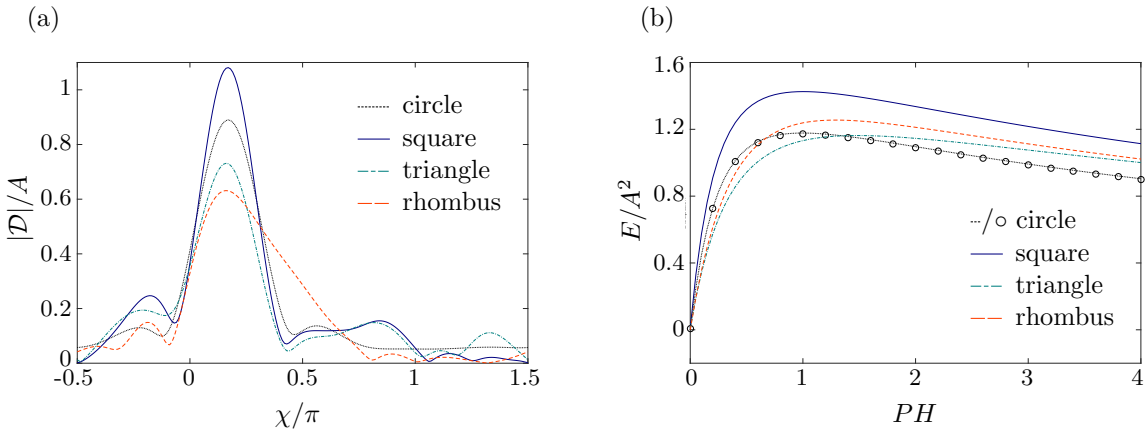

Figure 10: (a) Moduli of scattered far-field amplitude functions for different plate shapes, with porosity $PH = 0.5$ and incident angle $\psi = \pi/6$. (b) Energy dissipated due to porosity as a function of the porosity parameter, for different plate shapes. For the circular plate, the broken line is calculated using the eigenfunction-matching method and the symbols are calculated using the coupled boundary-element and finite-element method.

increases. The square plate, which covers the greatest area of the water surface, produces the most dissipation over the range of porosities considered. The circular plate, which covers the second greatest area, produces the second most dissipation for approximately $PH < 0.6$, but the least dissipation for approximately $PH > 1.4$. The rhombic plate produces more dissipation than the triangular plate, which covers the same area, although they dissipate almost identical amounts for the largest values of the porosity parameter considered.

6. Conclusions

Two solution methods have been outlined for the problem of water wave scattering by a floating porous elastic plate in three dimensions. A computationally efficient eigenfunction-matching method was developed for a plate of circular shape, requiring complex-valued wave numbers to be located. A more numerically costly coupled boundary-element and finite-element method was developed for a plate of arbitrary shape. For a circular plate, the coupled boundary-element and finite-element method was shown to produce the same plate displacements and scattered far field as the eigenfunction-matching method.

A representation of the far field as an integral of plane waves over the directional spectrum was used to investigate the impacts of porosity on the reflection and transmission produced by the plate. It was shown that porosity damps transmission in the direction of the incident wave, but increases scattering in all other directions. The rate of wave energy dissipation due to porosity was found not to monotonically increase as the plate became more porous, but, rather, to attain a maximum value for a finite value of the porosity parameter and then slowly decrease as the porosity increased. Moreover, the strength of the porosity was found to depend on the shape of the plate.

Acknowledgments

The U.S. Office of Naval Research supports MHM (N00014-13-1-0290). The Australian Research Council funds an early-career fellowship for LGB (DE130101571). The Australian Antarctic Science Program provides funding support for LGB (Project 4123). The University of Adelaide generously hosted MAP for a sabbatical, during which this work was accomplished.

An, S., Faltinsen, O. M., 2012. Linear free-surface effects on a horizontally submerged and perforated 2D thin plate in finite and infinite water depths. Appl. Ocean Res. 37 (7491), 220–234.

Behera, H., Sahoo, T., 2015. Hydroelastic analysis of gravity wave interaction with submerged horizontal flexible porous plate. J. Fluids Struct. 54, 643–660.

Bennetts, L. G., Biggs, N. R. T., Porter, D., 2007. A multi-mode approximation to wave scattering by ice sheets of varying thickness. J. Fluid Mech. 579, 413–443.

Bennetts, L. G., Biggs, N. R. T., Porter, D., 2009. Wave scattering by an axisymmetric ice floe of varying thickness. IMA J. Appl. Math. 74, 273–295.

Bennetts, L. G., Williams, T. D., 2010. Wave scattering by ice floes and polynyas of arbitrary shape. J. Fluid Mech. 662, 5–35.

Cho, I. H., Kim, M., 2008. Wave absorbing system using inclined perforated plates. J. Fluid Mech. 608, 1–20.

Cho, I. H., Kim, M. H., 2013. Transmission of oblique incident waves by a submerged horizontal porous plate. Ocean Eng. 61, 56–65.

Cho, I. H., Koh, H. J., Kim, J. R., Kim, M. H., 2013. Wave scattering by dual submerged horizontal porous plates: Further results. Ocean Eng. 73, 149–158.

Chwang, A. T., Chan, A. T., 1998. Interaction Between Porous Media and Wave Motion. Ann. Rev. Fluid Mech. 30 (1), 53–84.

Chwang, A. T., Wu, J., 1994. Wave scattering by a submerged porous disk. J. Eng. Mech. 120 (12), 2575–2587.

Evans, D. V., Peter, M. A., 2011. Asymptotic reflection of linear water waves by submerged horizontal porous plates. J. Eng. Math. 69 (2), 135–154.

Fox, C., Squire, V. A., 1994. On the oblique reflexion and transmission of ocean waves at shore fast sea ice. Phil. Trans. R. Soc. Lond. A. 347, 185–218.

Hassan, M., Meylan, M. H., Peter, M. A., 2009. Water-wave scattering by submerged elastic plates. Q. J. Mech. Appl. Math. 62 (3), 321–344.

Kaligatla, R. B., Koley, S., Sahoo, T., 2015. Trapping of surface gravity waves by a vertical flexible porous plate near a wall. Z. Angew. Math. Phys. 66 (5), 2677–2702.

Koley, S., Kaligatla, R. B., Sahoo, T., 2015. Oblique Wave Scattering by a Vertical Flexible Porous Plate. Stud. Appl. Math., 135 (1), 1–34.

Kumar, P. S., Sahoo, T., 2006. Wave Interaction with a Flexible Porous Breakwater in a Two-Layer Fluid. J. Eng. Mech. 132 (9), 1007–1014.

Linton, C. M., McIver, P., 2001. Handbook of Mathematical Techniques for Wave / Structure Interactions. Chapman & Hall /CRC.

Liu, Y., Li, H. J., Li, Y.-C., 2012. A new analytical solution for wave scattering by a submerged horizontal porous plate with finite thickness. Ocean Eng. 42, 83–92.

Liu, Y., Li, Y.-C., 2011. An alternative analytical solution for water-wave motion over a submerged horizontal porous plate. J. Eng. Math. 69 (4), 385–400.

Liu, Y., Li, Y.-C., Teng, B., 2007. Wave interaction with a perforated wall breakwater with a submerged horizontal porous plate. Ocean Eng. 34 (17-18), 2364–2373.

Liu, Y., Li, Y.-C., Teng, B., Dong, S., 2008. Wave motion over a submerged breakwater with an upper horizontal porous plate and a lower horizontal solid plate. Ocean Eng. 35 (16), 1588–1596.

Mandal, S., Behera, H., Sahoo, T., 2015. Oblique wave interaction with porous, flexible barriers in a two-layer fluid. J. Eng. Math., 1–31.

Mei, C. C., Stiassnie, M., Yue, D. K.-P., 2005. Theory and applications of ocean surface waves. World Scientific.

Meylan, M. H., 2002. The wave response of ice floes of arbitrary geometry. J. Geophys. Res. 107 (C6).

Meylan, M. H., Squire, V. A., 1994. The response of ice floes to ocean waves. J. Geophys. Res. 99 (C1), 891–900.

Molin, B., 2011. Hydrodynamic modeling of perforated structures. Appl. Ocean Res. 33 (1), 1–11.

Montiel, F., Squire, V. A., Bennetts, L. G., 2015a. Evolution of directional wave spectra through finite regular and randomly-perturbed arrays of scatterers. SIAM J. Appl. Maths. 75, 630–651.

Montiel, F., Squire, V. A., Bennetts, L. G., 2015b. Reflection and transmission of ocean wave spectra by a band of randomly distributed ice floes. Annals Glaciol. 56 (69), 315–322.

Neves, M. G., Losada, J. I., Losada, M. A., 2000. Short-wave and wave group scattering by submerged porous plate. J. Eng. Mech. 126, 1048–1056.

Newman, J. N., 1994. Wave effects on deformable bodies. Appl. Ocean Res. 16, 45–101.

Peter, M. A., Meylan, M. H., 2004. Infinite-depth interaction theory for arbitrary floating bodies applied to wave forcing of ice floes. J. Fluid Mech. 500, 145–167.

Peter, M. A., Meylan, M. H., Chung, H., 2004. Wave scattering by a circular elastic plate in water of finite depth: a closed form solution. Int. J. Offshore Polar Eng. 14 (2), 81–85.

Squire, V. A., 2008. Synergies between VLFS hydroelasticity and sea ice research. Int. J. Offshore Polar Eng. 18, 1–13.

Taylor, G., 1956. Fluid flow in regions bounded by porous surfaces. Proc. Roy. Soc. A, 456–475.

Tuck, E., 1975. Matching problems involving flow through small holes. Adv. Appl. Mech. 15, 89–158.

Wang, C. D., Meylan, M. H., 2004. A higher-order-coupled boundary element and finite element method for the wave forcing of a floating elastic plate. J. Fluids Struct. 19 (4), 557–572.

Wang, K.-H., Ren, X., 1993. Water waves on flexible and porous breakwaters. J. Eng. Mech. 119 (5), 1025–1047.

Wang, K. H., Shen, Q., 1999. Wave motion over a group of submerged horizontal plates. International Journal of Engineering Science 37 (6), 703–715.

Williams, A. N., Wang, K.-H., 2007. Flexible porous wave barrier for enhanced wetlands habitat restoration. J. Eng. Mech. 129, 260–263.

Wu, J., Wan, Z., Fang, Y., 1998. Wave reflection by a vertical wall with a horizontal submerged porous plate. Ocean Eng. 25 (9), 767–779.

Yip, T. L., Chwang, A. T., 2000. Perforated wall breakwater with internal horizontal plate. J.Eng. Mech. 126 (5), 533–538.

Yip, T. L., Sahoo, T., Chwang, A. T., 2002. Trapping of surface waves by porous and flexible structures. Wave Motion 35 (1), 41–54.

Yu, X., 2002. Functional performance of a submerged and essentially horizontal plate for offshore wave control: a review. Coastal Eng. 44 (2), 127–147.